

A Compact Implantable MIMO Antenna For High Data Rate Biotelemetry Applications

Amjad Iqbal, *Student Member, IEEE*, Muath Al-Hasan, *Member, IEEE*, Ismail Ben Mabrouk, *Senior Member, IEEE* and Mourad Nedil, *Senior Member, IEEE*

Abstract—This paper presents a low-profile multiple-input multiple-output (MIMO) implantable antenna system including a capsule endoscopy and a scalp implantation at Medical Implant Communication Service (MICS) band (402–405 MHz), and Industrial, Scientific, and Medical (ISM) band (433.1–438.8 MHz). It consists of two elements with an edge-to-edge gap of $0.0018\lambda_g$ and overall dimensions of $\pi \times (5.65)^2 \times 0.13 \text{ mm}^3$ and is placed on a 0.13 mm thick RO3010 ($\epsilon_r = 10.2$, $\tan\delta = 0.0022$) substrate. The antenna is integrated with batteries, sensors, and electronic components in two different types of implantable devices (capsule and flat-type devices). The simulation result shows that the antenna has a fractional bandwidth (FBW) of 33.9%, a maximum realized gain of -30 dBi, and isolation of more than 26 dB. The fabricated prototype is measured in a saline solution and minced pork meat. The measured results are found in good accordance with simulations. The antenna parameters are calculated and showed a significant independence between the radiators. A link budget is estimated to be 78 Mb/s for a distance of 20 meters. Thus, the proposed antenna is considered as a promising solution for high data-rate medical applications such as capsule endoscopy, live surgeries, and other biomedical applications where the high data-rate is required.

Index Terms—Bio-telemetry, channel capacity, implantable antenna, ISM band, link budget, MICS, MIMO.

I. INTRODUCTION

THE demand of using implantable electronic medical devices for health care and monitoring applications, such as capsule endoscopy, glucose monitoring, cardiac pacemakers, intra-oral tongue-drive system, and intracranial pressure monitoring, have been rapidly increased over the past few years [1]-[4]. This is due to the fact that implantable medical devices are capable of extracting biosignal features from various organs of the human body and transmitting the required information to the receiver [5]. In fact, the receiving device, that collects the information, can be placed either on the body or a couple of meters away from the human body. The implantable medical device can have many electronic and RF components such as sensors, batteries, filters, and antennas [6]. Indeed, the antenna is considered as an important component for high and efficient

data transmission between the implantable medical device and the receiver that is either wearable or located a few meters away from the human body [4].

However, implantable antenna design faces several challenges such as: (1) the large antenna size, which leads to a large implantable device, (2) the lossy nature of the human body's tissues, which greatly affects the functionality of the implantable antenna, (3) the relative permittivity of the human body's tissue, that is greater than the free space. As a result, the performance of the implantable antenna is dissimilar from the conventional free-space antenna [7]. Therefore, the performance of the implantable antenna in terms of the radiation properties in such sensitized domain requires to be consent with numerous conditions such as safe input power and Specific Absorption Rate (SAR) [4].

Recently, several research works have reported the design and test of implantable antennas performance, which include dual/multiple-band antennas [2]-[3], and ultra-wideband antennas [4]. However, all of these studies are single-input single-output (SISO) designs with relatively large sizes. Also, the spectral efficiency of these designs is relatively low inside heterogeneous human environment. Recently, a wideband antenna is introduced for high data-rate transmission. Nevertheless, the human body tissues are frequency-dependent, and hence, the electromagnetic properties are greatly affecting the antenna performance at high frequencies [8]. For instance, the tissues become more conductive and lossy with increasing the operating frequency. Also, the path loss increases with increasing the operating frequency, which significantly reduces the communication range, especially, for high data rates communication [4]. Furthermore, the wideband operation of implantable devices may interfere with nearby frequency bands. Therefore, a wideband antenna is not a good option to tackle the problem of low spectral efficiency in SISO topology. In order to overcome this drawback, MIMO systems have been recently proposed to enhance the spectral efficiency of implantable antennas [9]. Furthermore, the MIMO system also enhances the channel capacity without consuming any extra power or frequency resources [10]. Multiple antenna elements are used in MIMO systems to work as both transmitter and receiver, which improve the spectral efficiency. In fact, it has been demonstrated that MIMO are well suited to achieve higher throughput gain over SISO systems for capsule endoscopic application [9],[11]. Moreover, a dual-port antenna at MedRadio band for high data rate implantable devices with an adequate FBW of 35.9% is studied in [12]. In [13], an electromagnetic band-gap (EBG) based four-element

This work was supported by the Abu-Dhabi Department of Education and Knowledge (ADEK) Award for Research Excellence 2019 under Grant AARE19-245. (Corresponding Author: Amjad Iqbal.)

A. Iqbal and I. Ben Mabrouk are with the Department of Engineering, Durham University, Durham DH1 3LE, UK (e-mail: ismail.benmabrouk@durham.ac.uk)

M. Al-Hasan is with the Network and Communications Engineering Department, Al Ain University, Al Ain, United Arab Emirates (e-mail: muath.alhasan@aau.ac.ae).

Mourad Nedil is with the Communications Research Laboratory (LRTCS), University of Quebec at Abitibi-Temiscamingue (UQAT), Val-d'Or, QC J9P 1Y3, Canada (e-mail: mourad.nedil@uqat.ca).

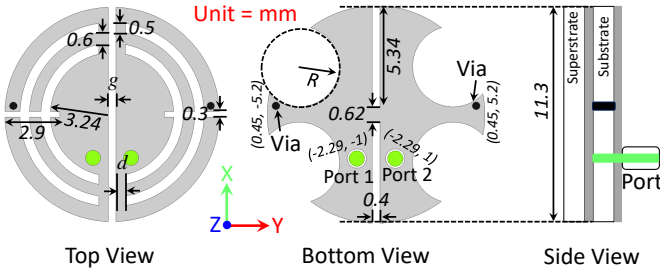


Fig. 1: Top ($g = 0.4$ mm, and $d = 0.5$ mm), bottom ($R = 1.1$ mm), and side view of the proposed antenna (Unit = mm).

implantable MIMO antenna is introduced for 2.4 GHz ISM band with a narrow FBW of 18.64%. In [14], a four-element MIMO cubic implantable antenna is proposed. However, the non-planar and large footprint make its applications limited for compact implantable medical devices. The majority of the reported MIMO implantable designs have large antenna sizes which restrict to implement them in compact implantable devices.

In this paper, a novel design of implantable MIMO antenna system is presented. It can significantly enhance the spectral efficiency without any extra power or frequency resources. The miniaturization of the proposed design is achieved by using shorting pins, loading rectangular and arc-shaped slots on the radiator, and open-ended circular slots on the ground plane. The antenna is simulated and measured in a quasi-implantable device with considering batteries, sensors, lumped elements and substrates. To the authors' knowledge, this is the first ever MIMO antenna system which is simulated and measured inside a quasi-implantable device.

II. DESIGN METHODOLOGY

Fig. 1 shows the proposed two ports MIMO antenna which consists of radiating patches, partial ground structures, a substrate and a superstrate. Each radiating patch consists of a semi-circular patch with one rectangular and two arc-shaped slots. Both radiating patches have the same ground plane as depicted in Fig. 1. A small edge-to-edge distance of $0.0018\lambda_g$ (where, λ_g is the guided wavelength at 433 MHz) is kept between the radiators. In fact, the medium around the substrate is air in both implantable devices. Therefore, λ_g only takes into account the permittivity of the antenna's substrate ($\epsilon_r = 10.2$). The ground plane has a circular shape with two inverted rectangular slots and four circular slots. Each radiating patch is excited with a 50Ω coaxial cable with a diameter of 0.8 mm at feed point of $(0.45, -5.2/0.45, 5.2)$ in the Cartesian coordinate system. A shorting pin of diameter of 0.5 mm is used in each radiating patch to lower down the operating frequency. An ultra-thin material (thickness = 0.13 mm) of Rogers RO3010 ($\epsilon_r = 10.2$, $\tan\delta = 0.0022$) is used as a substrate and superstrate. The superstrate assists in insulating the antenna from direct interaction with the components of the implantable devices [4].

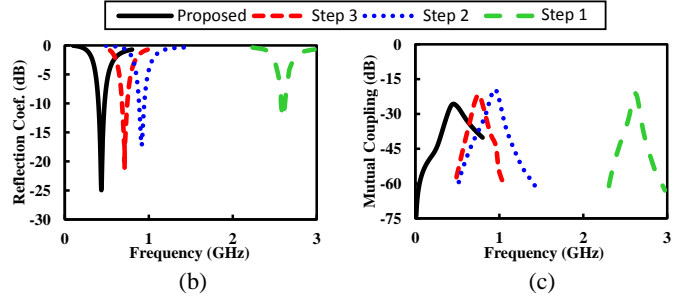
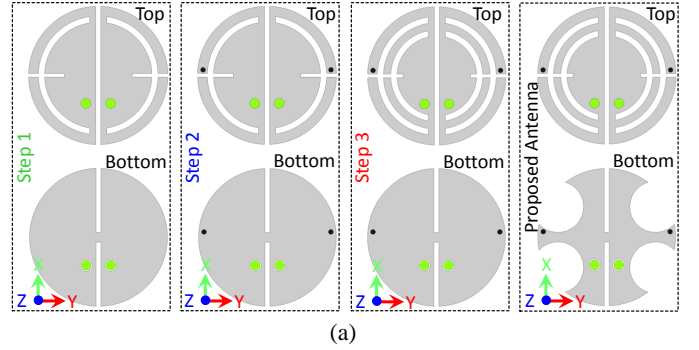


Fig. 2: (a) Evolution stages (design steps) of the proposed antenna, (b) reflection coefficient (S_{11}) in evolution stages, and (c) mutual coupling (S_{21}) in evolution stages.

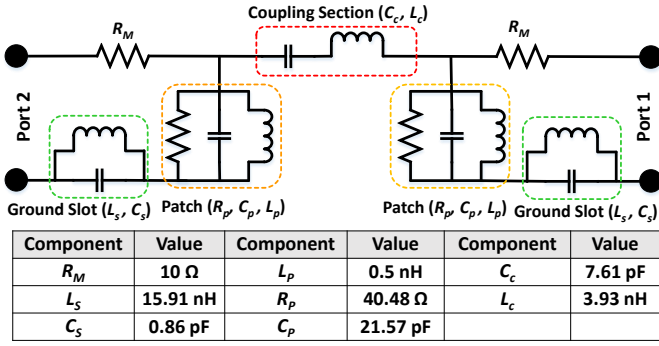
A. Design Evolution (Miniaturization and Bandwidth Improvement)

An iterative process for achieving the desired results consists of four stages, as illustrated in Fig. 2a. Fig. 2b and 2c show the scattering parameters (S_{11} and S_{21}), respectively. Initially (Step 1), a semi-circular radiating patch with one rectangular slot and one arc-shaped slot is designed with the circular ground plane. The initial dimensions are calculated using Equation (1) [15]. The rectangular slot and an arc-shaped slot are loaded on the patch to expand the current path and induce capacitive effect, thereby, reducing the patch's resonant frequency [16]. Theoretically, the equivalent circuit of an antenna can be modeled as a series inductance (L_o) and shunt capacitance (C_o), as an ideal transmission line. The propagation velocity (v_p) can be calculated using Equation (2) [16]. It can be seen that v_p has inverse relationship with the capacitance (C_o) and inductance (L_o). The rectangular and arc-shaped slot add additional capacitance to the antenna [17]. By adding them, the overall capacitance of the antenna is increased. Hence, the value of v_p is decreased and miniaturization is achieved.

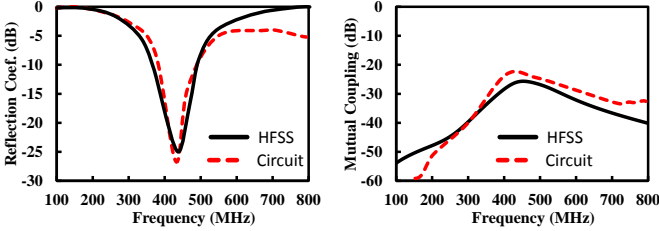
$$f_{res} = \frac{1.8412 \times c}{4\pi R_a \sqrt{\epsilon_r}} \quad (1)$$

where f_{res} is the resonant frequency of the circular radiating patch, ϵ_r is the substrate relative permittivity of 10.2, R_a is the radius of the circular patch, c is the speed of light (3×10^8 m/s), and h is the thickness of the substrate.

$$v_p = \frac{1}{\sqrt{L_o C_o}} = \frac{c}{\sqrt{\epsilon_{eff}}} = \lambda_g f \quad (2)$$



(a)

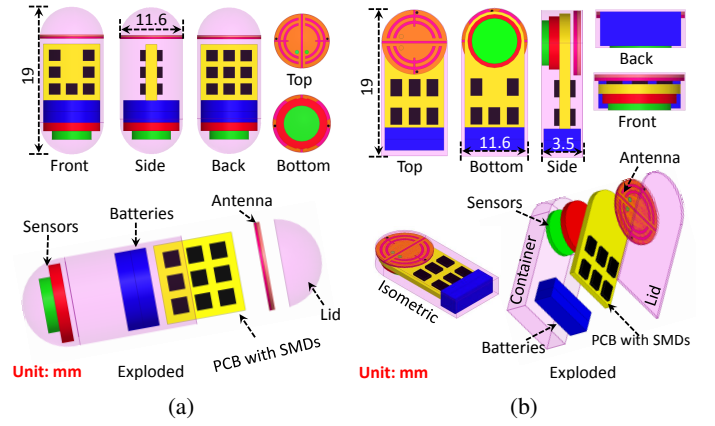


(b)

(c)

Fig. 3: (a) Equivalent lumped element circuit model of the proposed antenna (b) reflection coefficient results of both (HFSS and circuit) model, and (c) mutual coupling results of both model.

The resonant frequency of the antenna in step 1 is 2.6 GHz with a narrow 10-dB bandwidth. A FBW of 1.1 % is observed in step 1. The resonant frequency is reduced by adding a shorting pin. The shorting pin has a diameter of 0.5 mm. As a result, the resonant frequency is shifted from 2.6 GHz to 0.914 GHz. A FBW of 10.9 % is observed in step 2. In step 3, a second arc-shaped slot is also loaded to the radiating patch, which further increases the current path. Hence, the resonant frequency is shifted from 914 MHz to 712 MHz. A FBW of 20.9 % is achieved in step 3. In step 4, four circular slots are etched in the ground plane. In fact, the open-ended slots are mostly used to enhance impedance matching, to shift resonant frequencies to lower frequencies (miniaturization), and to generate multi-bands [4],[18]. Moreover, an open-ended ground slots are added to achieve miniaturization, impedance matching, and also bandwidth improvement. The resonant frequency is shifted from 712 MHz to 433 MHz by introducing slots in the ground plane. A FBW of 33.9 % (355–500 MHz) is observed in step 4, as shown in Fig. 2b. The aim of using open-ended slots in the ground plane is justified by the enhancement of the impedance matching, improvement of the bandwidth and achievement of the miniaturization. Hence, the resonant frequency is shifted from 2.6 GHz to 433 MHz, with a bandwidth improvement from 1.1% to 33.9%, and an impedance matching enhancing from -12.5 dB to -25.9 dB through the design evolution process. Fig. 2c shows S_{21} results of the antenna in each step. It can be seen that in each step, the isolation is better than 17 dB in the whole operational band throughout the design evolution process. The isolation in the final step (final antenna design) is higher than 26 dB in



(a)

(b)

Fig. 4: The detail architecture of implantable devices (a) capsule-type for deep tissue implant, and (b) flat-type for skin implant.

the whole operational band, even with a smaller edge-to-edge distance of $0.0018\lambda_g$ between the radiators.

B. Equivalent Circuit Model

In order to include a detailed analysis of the proposed design, a lumped element equivalent circuit model is shown in Fig. 3a. The equivalent circuit model is designed using Keysight Advanced Design System (ADS). Each radiator is excited with a 50Ω terminal and modeled as a parallel RLC circuit (R_p , C_p , and L_p) [19]. R_p , C_p , and L_p values depend on the radiator parameters such as the radiator's radius and the slot dimensions. The circular slots in the ground plane are also modeled as a parallel LC circuits (L_s , and C_s). The values of L_s and C_s depend on the circular slot's dimensions in the ground plane. The undesirable coupling between the two radiators is modeled as a series LC circuit (L_c and C_c), which mainly depends on the gap between the radiators and inverted rectangular slots in the ground plane. The optimized values of the equivalent circuit model are shown in Fig. 3a. Fig. 3b and 3c compare the simulated S_{11} and S_{21} of the electromagnetic (EM) model (HFSS) and circuit model (ADS), respectively. A close match between both models is observed.

C. System Architecture (Capsule and Flat-type Device Design)

Every implantable biomedical device has a specific implantation area and device architecture. Most studies reported either capsule-type or flat-type device architecture for system-level consideration. In this manuscript, both architectures are studied and discussed. Fig. 4a and 4b show the system architecture of the capsule-type and flat-type implantable device, respectively. The capsule-type device, having a length of 19 mm and a radius of 5.8 mm, is considered for deep tissue implantation, as shown in Fig. 4a. The flat-type device, having dimensions of $11.6 \times 11.6 \times 3.5$ mm³, is studied for skin implantation, as illustrated in Fig. 4b. Each implantable device consists of the proposed MIMO antenna, batteries, sensors, and a PCB with surface mounted devices (SMDs). Different resistors, inductors and capacitors are added on the PCB as

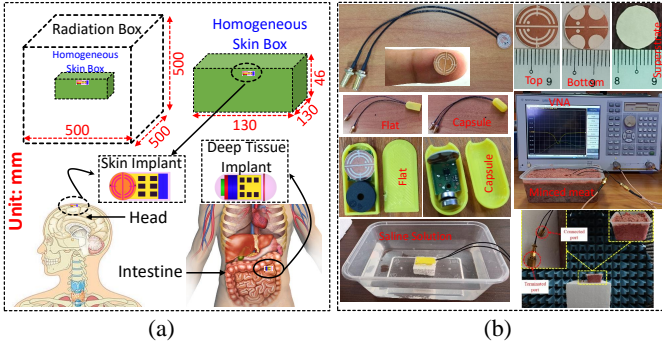


Fig. 5: (a) Simulation setups and (b) fabricated prototype and measurement setups.

a dummy electronic components during simulations. A 0.1 mm thick biocompatible material having $\epsilon_r = 9.8$ and $\tan\delta = 0.006$ is used as a casing for both devices. The casings of both devices are tightly closed with epoxy to avoid entering liquid in the device during experimental measurements.

D. Simulation Environment and Measurement Setups

At the start of the design procedure, the proposed implantable MIMO antenna is simulated and optimized using HFSS in a one-layer homogeneous skin model. The dimensions of one-layer homogeneous skin model is $130 \times 130 \times 46$ mm³. The electrical characteristics of one-layer skin model is selected as $\epsilon_r = 46.08$, $\sigma = 0.702$ S/m for 433 MHz (ISM band), according to [2]. The antenna is implanted at a depth of 4 mm from the top. The far-field radiation box is designed at more than $\lambda_0/4$ (overall dimensions of $500 \times 500 \times 500$ mm³) from edges of the antenna at the resonant frequency (433 MHz), as shown in Fig. 5. In addition, the proposed implantable MIMO antenna is integrated with a full-package device (capsule and flat-type device). The implanted depth is set to 4 mm in a homogeneous skin model, and in the head of a human body. However, the implanted depth in the large intestine is fixed to 90 mm.

To validate the simulation results, the proposed implantable MIMO antenna is fabricated on the ultra-thin substrate of Rogers RO3010 ($\epsilon_r = 10.2$, $\tan\delta = 0.0022$, and height of the substrate = 0.13 mm). A dummy electronic PCB is fabricated using FR-4 substrate and SMDs are soldered over it. The capsule and flat-type devices are designed using 3D printing technology. The components such as implantable antenna, sensors, batteries, and single-layer PCB are carefully enclosed (using epoxy) in the device to measure the results (S_{11} , S_{21} , radiation pattern, gain and received power). The S_{11} and S_{21} results of the fabricated antenna are measured in a saline solution and minced pork meat using an Agilent Technologies vector network analyzer (VNA) model E5062A. The radiation patterns and gain are measured in an anechoic chamber. The whole antenna system is embedded into the minced pork meat. The antenna is placed in the middle of a container containing minced pork meat at a depth of 4 mm. A signal generator, high-gain horn antenna and spectrum analyzer are used to measure the radiation pattern. The high-gain horn antenna

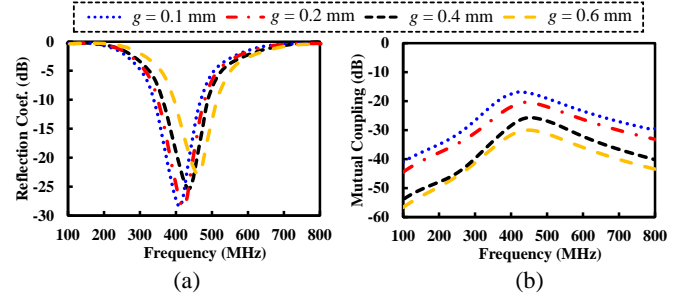


Fig. 6: S-parameters of the antenna as a function of varying parameter g (a) reflection coefficient, and (b) mutual coupling.

(width = 49 cm, depth = 40 cm, and height = 32 cm) is used for transmitting and our proposed implantable antenna for receiving the incoming power. One port of the implantable MIMO antenna is connected to the spectrum analyzer and the second port is terminated with a 50Ω load. A distance of 3 meters is kept between the edge of the horn antenna and the proposed antenna. A high-gain horn antenna is powered and the proposed antenna is rotated with a step size of 10° to measure the incoming power.

E. Parametric Study

To achieve better performance of the proposed antenna, various important parameters that can affect the reflection coefficient and the mutual coupling of antenna are analyzed. When the key parameter is studied, the others are kept constant. To investigate the effect of the gap (g) between the radiating elements on the the antenna S-parameters, the value of g is varied and the results are shown in Fig. 6. It can be observed that the MIMO elements are disconnected and there is no direct path for the fields to travel from one patch to the second one. However, both patches are capacitively coupled. The mutual coupling is dependent on the value of g and has an inverse relationship with it. Moreover, it can be observed that the mutual coupling increases with reducing the value of g . In fact, the coupling level becomes dominant when the patches are closer. Furthermore, when g increases, the effective radiating area of the patch reduces. As a result, the resonant frequency shifts to the higher frequencies, as shown in Fig. 6. Besides, the parameter d shows a significant impact on the resonant frequency of the antenna. When d increases, the lengths of the arc-shaped slots reduce. In fact, the arc-shaped slots provide an extra capacitance to the patch. Therefore, by increasing the value of d (reducing the lengths of the arc-shaped slots), the capacitance of the patches reduces which allow shifting the resonant frequency to the higher frequencies, as illustrated in Fig. 7a. The effect of d is further verified by the equivalent circuit model. The capacitance of the patch is 21.5 pF when the value of d is 0.5 mm; However, this value is decreased to 16.42 pF when d is 3.5 mm (Fig. 7). It is worthy mentioning that the rest of the circuit components are same for all values of d , which confirms that d has only an impact on the capacitance of the patch (C_p). Furthermore, it has a negligible impact on the mutual coupling of the antennas, as shown in Fig. 7b. On the other hand, the radius (R) of the open-

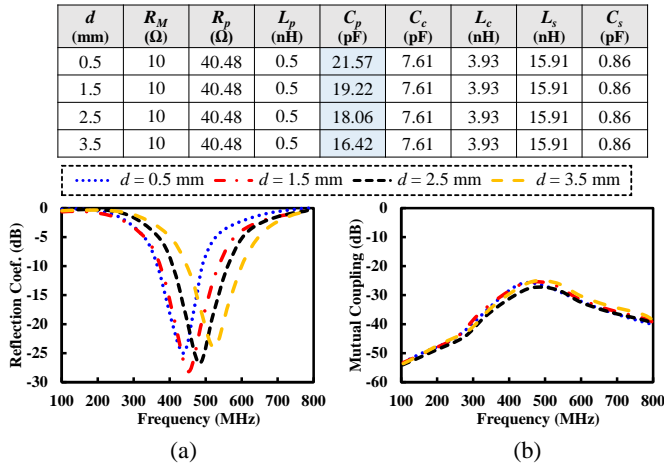


Fig. 7: S-parameters of the antenna as a function of varying parameter d (a) reflection coefficient, and (b) mutual coupling.

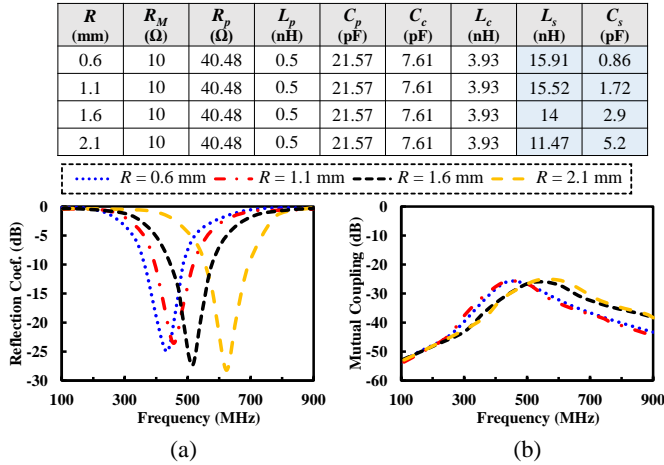


Fig. 8: S-parameters of the antenna as a function of varying parameter R (a) reflection coefficient, and (b) mutual coupling.

ended ground slot has an impact on the resonant frequency and fractional bandwidth of the antenna. The open-ended slot adds additional capacitance to the patch, which allow shifting the resonant frequency to the lower band. Also, the open-ended slot reduces the equivalent inductance of the antenna which enhances the fractional bandwidth. It is observed that the resonant frequency is shifted to the higher frequency side by reducing the value of R , as shown in Fig. 8a. Furthermore, the fractional bandwidth is enhanced with an increase in R . The effect of the open-ended slot is further verified by the equivalent circuit model. It can be observed that R has an inverse relationship with the inductance (L_s) and has a direct impact on the capacitance (C_s). Similarly, the rest of the circuit components are same for all values of R , which confirms that R has only an impact on the ground capacitance (C_s) and ground inductance (L_s). Furthermore, it has a minor effect on the antennas' mutual coupling (Fig. 8b).

Apart from an antenna, an implantable device contains batteries, microchips, resistors, inductors, PCB, capacitors, and sensors [20]. These components can couple with the antenna and affect its performance, especially in terms of

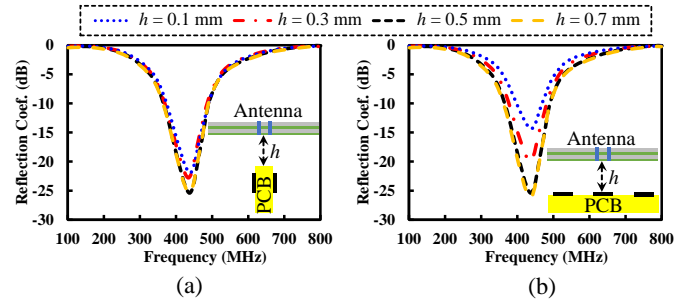


Fig. 9: Effects of electronic components and PCB on the reflection coefficient of the antenna in (a) capsule-type device, and (b) flat-type device.

impedance matching and radiation properties. The antenna should be placed in such a way as to have minimal coupling with other components of the implantable device. Therefore, it is necessary to investigate the coupling effects of the PCB and its electronic components with the implantable antenna to obtain a minimum gap between them. To investigate the coupling effects, the gap (h) between the antenna and PCB is varied from 0.1 mm to 0.7 mm. As illustrated in Fig. 9, the coupling effect of PCB and electronic components in the capsule-type implantable device is almost negligible because these components are placed vertically below the antenna and have minimal coupling region. In the case of a flat-type implantable device, the coupling effect increases by reducing the gap between the antenna and the PCB. To have wide bandwidth and better impedance matching, a minimum gap of 0.5 mm is maintained between the antenna and the PCB.

III. RESULTS AND DISCUSSIONS

The antenna design performance is analyzed in a single layer homogeneous skin model to reduce the simulation time. After that, the antenna's sensitivity is checked by examining the antenna with a full human body phantom in different parts of the body (head and large intestine). The simulated reflection coefficient and transmission coefficient is validated by measuring the fabricated antenna in a saline solution and minced pork meat. The simulated (homogeneous skin model, realistic human head, and large intestine) and measured (saline solution and minced pork meat) S_{11} and S_{21} results are illustrated in Fig. 10a and Fig. 10b, respectively. It can be observed that the proposed antenna resonates at 433 MHz, covering important MICS (402–405 MHz) and ISM (433.1–438.8 MHz) bands. The antenna resonates at 433, 429, 428, 435, and 430 MHz with a fractional bandwidth of 33.9% (355–500 MHz), 35.8% (349–501 MHz), 21.7% (386–480 MHz), 31.3% (363–498 MHz), and 31.2% (362–495 MHz) in a homogeneous skin model, large intestine, human head, minced pork meat (measured), and saline solution (measured), respectively. The simulated S_{21} values are lower than -26 dB in the operation band while the measured values are lower than -22 dB, as shown in Fig. 10b. The measured S_{21} values are higher due to two possible reasons: (1) soldering of coaxial cables, which increases copper portion of the antenna and facilitates surface waves to travel from one port to another,

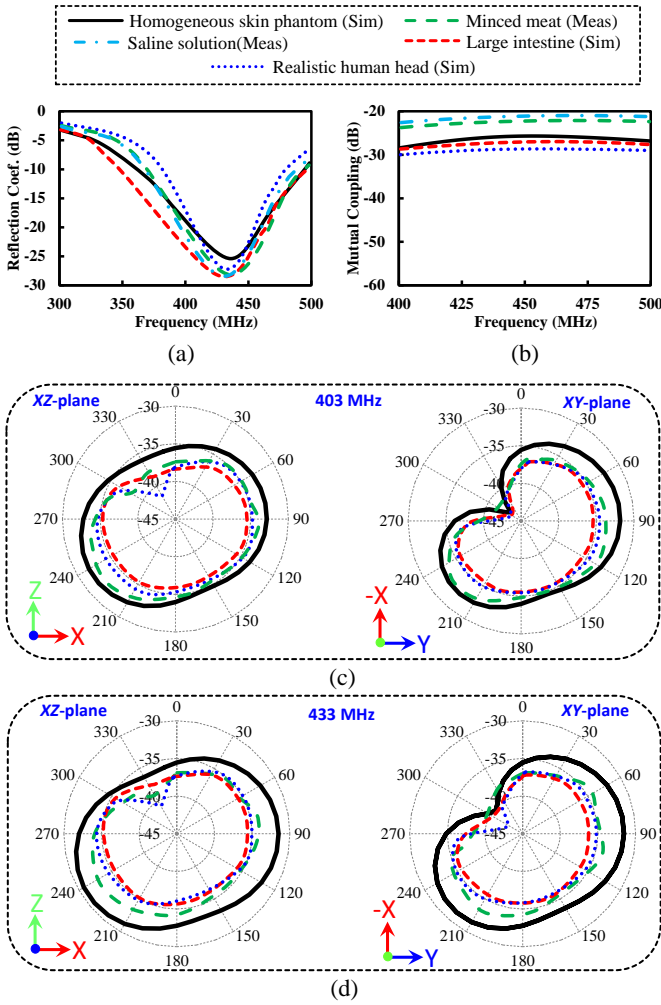


Fig. 10: Simulated and measured results of the antenna in different simulation environments (a) S_{11} , (b) S_{21} , (c) radiation patterns at 403 MHz when one port is excited and other is terminated with a 50Ω impedance, and (d) radiation patterns at 433 MHz when one port is excited and other is terminated with a 50Ω impedance.

and (2) reactive fields of the coaxial cables. It is known that mutual coupling significantly affect the antenna parameters (gain, radiation pattern and bandwidth) [21]. In fact, the mutual coupling between the antenna elements can be reduced by reducing either surface waves or near-field coupling or both. An ultra-thin (0.13 mm) substrate is chosen to restrict the transmission of the surface-waves [21]. Hence, the mutual coupling is reduced to the minimum level.

The antenna radiation patterns in XY - and XZ -plane are measured at 403 and 433 MHz in an anechoic chamber. The radiation patterns are measured by placing the antenna system inside the minced pork meat. It is known that the antenna is fed by other RF front-ends inside the human body in real applications. Therefore, the implantable antenna in this study is enclosed by waterproof casing with full electronic package devices. It can be noticed, from the antenna's radiation patterns, that the radiation patterns of the antenna are almost identical at 403 and 433 MHz, as shown in Fig. 10c-d. In fact,

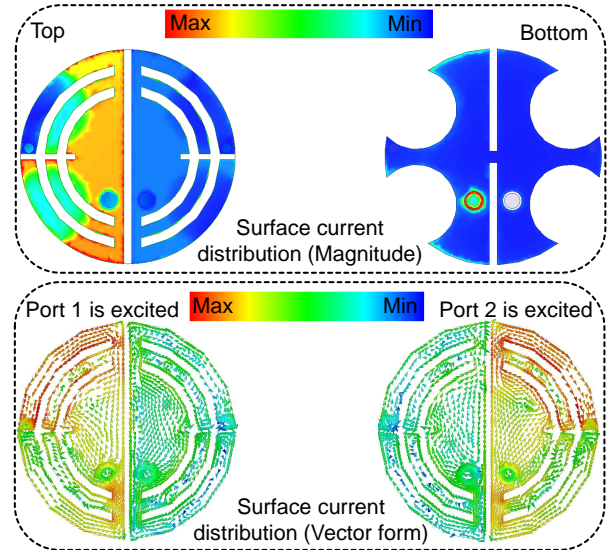


Fig. 11: Surface current distribution of the antenna at 433 MHz.

the maximum beam is oriented towards the X -axis and Y -axis directions at 403 MHz and 433 MHz. Therefore, any metallic components in the X -axis and Y -axis directions of the antenna will disturb the radiation pattern. The simulated maximum realized gains of -30, -35.6 and -34.8 dBi are observed in the homogeneous skin model, large intestine, and human head, respectively. The measured maximum gain is found to be -34.4 dBi. Moreover, the radiation efficiencies of -36.7, -39.1 and -37.4 dB are observed in a skin model, large intestine, and human head, respectively.

The surface current distribution study is conducted to understand the coupling intensity phenomenon between the radiators. The surface current distribution of the antenna system is shown in Fig. 11, when port 1 is excited. It can be seen that the current is quasi-evenly distributed over the excited patch. It can also be noticed that almost zero current is coupled with the second antenna. The current level of the excited element is higher than the non-excited element even with a smaller edge-to-edge distance of $0.0018\lambda_g$, where λ_g is the guided wavelength at 433 MHz. Furthermore, the current intensity on the ground plane below the radiator (left part of the ground plane) is higher than the right part of ground plane, which further confirms weak coupling between the radiators.

The SAR of the antenna is evaluated to ensure safety of the human body during the operation of implantable devices. We assessed the SAR results at 433 MHz over 10-g tissue in the realistic human head using a flat-type device and in the large intestine using a capsule-type device. Both antenna elements are excited with an input power of 1W. The peak SAR values of 538.6 W/Kg and 550.4 W/Kg are calculated at the human head and large intestine when both antenna elements are excited, as shown in Fig. 12. Therefore, due to one antenna element, the peak SAR values are 269.3 W/Kg and 275.2 W/Kg in the human head and large intestine, respectively. In practical cases, the implantable medical devices operate at input power of $< 25 \mu\text{W}$ (ITU Rec. ITU-R RS.1346) [22].

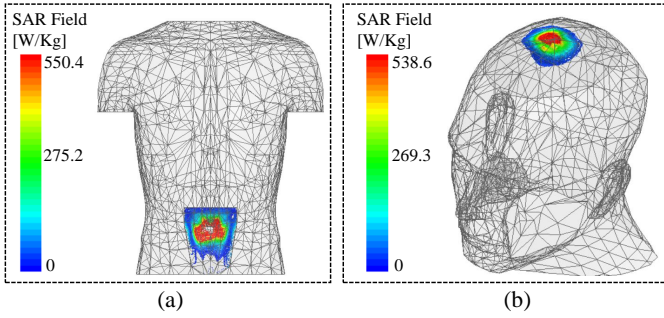


Fig. 12: SAR over 10-g tissue at 433 MHz, when both ports are powered with 1 W, in (a) large intestine and (b) human head.

Based on our calculated SAR, maximum allowable powers are 7.42 mW and 7.26 mW in the human head (flat-type device) and large intestine (capsule-type devices) to ensure SAR safety limits.

A. Link Budget For Wireless Communication

As mentioned, the proposed antenna is designed for high-data rate implantable devices. Therefore, it is important to evaluate the link budget parameters for effective communication between the implantable antenna and off-body/on-body receivers. A 20 dB margin is considered for a reliable communication. Link margin is the difference between available power and required power, and can be computed using Equation (3) [6].

$$LM[dB] = P_a - P_r \quad (3)$$

$$P_a[dB] = P_t + G_t + G_r - L_f - N_o \quad (4)$$

$$P_r[dB] = \frac{E_b}{N_o} + 10\log_{10}(B_r) - G_c + G_d \quad (5)$$

where

$$L_f[dB] = 10\log_{10}\left(\frac{4\pi a}{\lambda}\right)^2 \quad (6)$$

and

$$N_o = 10\log_{10}(kT_o) \quad (7)$$

In link budget calculations, an ideal $\lambda/2$ dipole antenna ($G_r = 2$ dBi) is considered as receiving antenna. Furthermore, losses due to polarization and impedance mismatches are neglected. The distance between the transmitter (implantable MIMO antenna) and receiver (ideal $\lambda/2$ dipole antenna) is denoted with d . The parameters of link budget are detailed in Table. I.

The calculated link budget is illustrated in Fig. 13. The link margin between the available and required powers must be higher than 0 dB to transmit the associated information over a suitable distance. However, we considered a link margin of at least 20 dB for error-free communication. We considered a low transmitted power of $P_t = 25 \mu\text{W}$ to avoid interference with other devices operating at the same frequency. It can be

TABLE I: PARAMETERS FOR LINK BUDGET ANALYSIS.

Variables	Description (Units)	Values
Transmitter Side		
f	Frequency (MHz)	433
P_t	Transmitted power (dBm)	-16
G_t	Implantable antenna gain (dBi)	-30
Receiver Side		
G_r	Receiver antenna gain (dBi)	2
T	Temprature (K)	273
k	Boltzmann constant	1.38×10^{-23}
N_o	Noise power density (dB/Hz)	-199.95
Signal Quality		
B_r	Bit rate (Mbps)	Various
G_c	Coding gain (dB)	0
G_d	Fixing deterioration (dB)	2.5
BER	Bit error rate	1×10^{-5}
E_b/N_o	Ideal PSK (dB)	9.6
Margin (dB) = $P_a - P_r$		

observed from the link margin plot that the communication range decreases with increase in the data rates. As a result, the proposed system can efficiently communicate up to 20 meters for a high data rate of 78 Mb/s. Such high data rate antenna system can be used for capsule endoscopy, surgeries, and other applications where high throughput for transmission is required. Additionally, an experiment is carried out to estimate the transmission ability of the fabricated antenna. Two software-defined radios (SDRs) platforms have been used in this experiment. The experimental setup is shown in Fig. 14a. The proposed antenna is used as a transmitting antenna and a high gain SDR antenna as a receiving one. Then, the antenna is connected to the SDR and a narrow frequency modulated (NFM) signal is generated at 433 MHz. The signal is transmitted from SDR through our proposed antenna. Another SDR having an antenna with a gain value of 2 dBi is used as a receiving antenna. The receiving SDR is connected with the Laptop to monitor the received power. The simulated and measured received power is shown in Fig. 14b. The simulated and measured received powers have around 2-3 dB difference which is reasonable as the real experimental environment is lossy as compared to the ideal scenarios [23]. The difference between the simulated and measured powers are due to cable losses, reflection losses, conductor and dielectric losses, mismatch losses, polarization loss factor, scattering losses and other environmental effects.

B. MIMO Channel Parameters

1) *Envelope Correlation Coefficient*: An envelope correlation coefficient (ECC) is considered as an important parameter in MIMO systems which verifies system independence in their separate performance. The ideal (desirable) value of ECC is zero, however, in practical applications, an $ECC < 0.5$ is also acceptable. In fact, ECC of a MIMO system can be

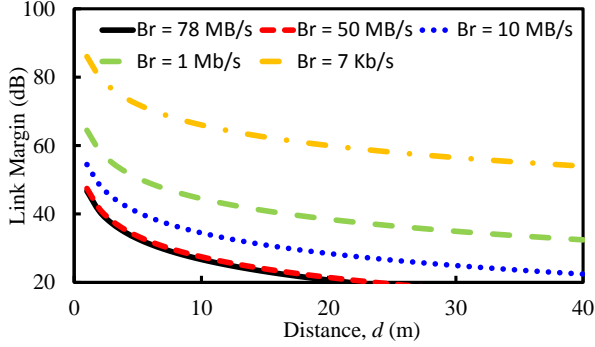


Fig. 13: Link margin for different transmission rates at 433 MHz.

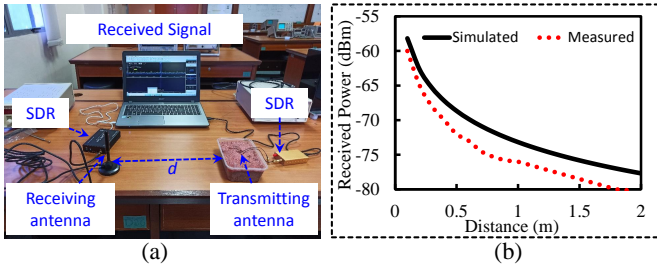


Fig. 14: (a) Experimental setup for measuring the received power, and (b) simulated and measured received power as a function of a distance between the antennas (d).

evaluated using S-parameters or far-field radiation patterns. In our study, ECC is computed using far-field patterns using Equation (8) [21], [24]. Here, ECC of the antenna is computed by considering antenna in a homogeneous skin model. The ECC values versus frequencies are plotted in Fig. 15a. It can be noted that the simulated ECC values are lower than 0.1 over the entire frequency band and is equal to 0.094 at 433 MHz. The measured ECC values are lower than 0.14 over the entire frequency band and is equal to 0.12 at 433 MHz. The ECC value is low enough to confirm the excellent diversity performance. Such low values of the ECC make this system suitable for high data rate implantable devices, such as modern capsule endoscopy.

$$ECC = \frac{|\iint_{4\pi} (\vec{A}\vec{n}_i(\theta, \phi)) \times (\vec{A}\vec{n}_j(\theta, \phi)) d\Omega|^2}{\iint_{4\pi} |(\vec{A}\vec{n}_i(\theta, \phi))|^2 d\Omega \iint_{4\pi} |(\vec{A}\vec{n}_j(\theta, \phi))|^2 d\Omega} \quad (8)$$

where $\vec{A}\vec{n}_i(\theta, \phi)$ is the 3D pattern of the i^{th} antenna and $\vec{A}\vec{n}_j(\theta, \phi)$ is the 3D pattern of the j^{th} antenna. Ω represents the solid angle in Equation (8).

2) *Diversity Gain*: Furthermore, diversity gain (DG) shows the impact of the diversity scheme on the transmitted power. An optimal value of DG is always 10 dB, which represent completely uncorrelated channels. DG of the antenna system is computed [21], which shows that DG is completely dependent on ECC values. The simulated DG values of the antenna against varying frequencies is shown in Fig. 15a. It is found that simulated DG of the antenna system is greater than 9.95 dB in the whole operating band and is equal to 9.96 dB at the

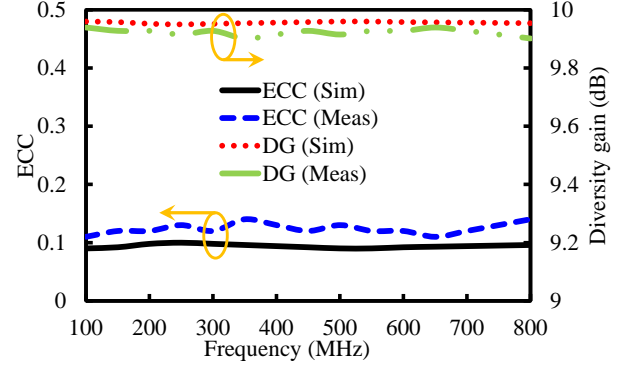


Fig. 15: MIMO channel parameters: ECC and Diversity gain of the MIMO antenna.

targeted band of 433 MHz. The measured DG of the antenna system is greater than 9.90 dB in the whole operating band.

3) *Channel Capacity and Cumulative Distribution Function*: The basic purpose behind MIMO antenna system is to enhance the channel capacity (CC) without using extra frequency spectrum and power resources. Considering uncorrelated channels, the CC of the antenna system increases with the number of transmitting and receiving antennas. Nevertheless, in real-time applications, fully uncorrelated channels are impossible. Indeed, the CC depends on the number of antennas and the correlation between channels. For high CC, more antennas are desirable with high isolation. The CC of an $N \times N$ MIMO antenna system is given as [25]:

$$CC = \log_2 \left(\det \left[I + \frac{SNR}{N} H H^* \right] \right) \quad (9)$$

where CC is the channel capacity, I is the identity matrix, H is the channel matrix which contain the information of gain and phase of the antennas and H^* is the conjugate of matrix H .

The CC of the antenna system can be estimated from the radiation patterns using real environment measurements or theoretical models. The authors of [26] designed a reverberation chambers to measured CC of the MIMO system. It provides the indoor and outdoor environment similar to the real environment. The CC can be measured inside this chamber without the real environment.

In [27], the authors provided a complete guide on estimating the CC of the MIMO antenna system. The CC of the MIMO antenna system can be calculated by deriving the channel matrix H from the 2D radiation patterns of the transmitting and receiving antennas. We used Equation (10) for calculating the channel matrix H [27].

$$H = \sqrt{\Psi_t} G \sqrt{\Psi_r} \quad (10)$$

where H is the channel matrix, G is the random matrix with Gaussian entries, Ψ_t is the transmit correlation matrix and Ψ_r is the receive correlation matrix. The correlation matrix can be computed using Equation (11) [27].

$$\Psi_r^{x,y} \text{ or } \Psi_t = \frac{\mu_{xy}}{\sqrt{\mu_{xx}\mu_{yy}}} \quad (11)$$

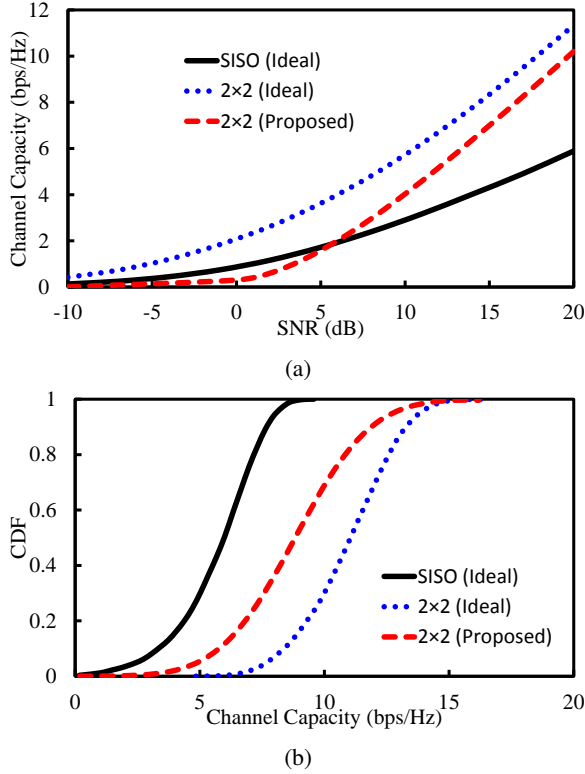


Fig. 16: MIMO channel parameters: (a) Average channel capacity as a function of SNR and (b) CDF as a function of channel capacity at an SNR value of 20 dB.

The values of $\mu_{x,y}$ can be calculated from 2D radiation patterns of antenna x and antenna y as [27];

$$\mu_{x,y} = \int_0^{2\pi} [XPD \times A_{x,\theta} A_{y,\theta}^* + A_{x,\phi} A_{y,\phi}^*] d\phi \quad (12)$$

where A_θ and A_ϕ are the radiation patterns of antenna x and antenna y and XPD is the cross-polarization discrimination.

The CC of the MIMO antenna system is calculated using 2D radiation patterns. The CC against varying Signal-to-Noise Ratio (SNR) is given in Fig. 16a. It can be noted that the CC of the proposed MIMO antenna system is lower than the ideal 2×2 MIMO system and more than ideal SISO system. Considering an SNR value of 20 dB, the ideal 2×2 MIMO system has CC of 11.34 bps/Hz, the proposed MIMO system has CC of 10.2 bps/Hz and the ideal SISO has CC of 5.89 bps/Hz. Cumulative distribution function (CDF) is derived at an SNR value of 20 dB and is shown in Fig. 16b. It can be seen that the proposed antenna has higher CC than ideal SISO system which is a promising solution for high data-rate medical applications.

The performance of the proposed antenna is compared with reported implantable MIMO antennas in Table. II. It can be noticed that the proposed antenna has the most compact size and the lowest mutual coupling compared to other antennas. Also, FBW of the proposed antenna is more than [9] and [12]. It is worthy mentioning that we have also studied the MIMO channel parameters to evaluate the independence of

TABLE II: COMPARISON WITH IMPLANTABLE MIMO ANTENNAS.

Parameters	[9]	[12]	[13]	This Work
Size (mm^3)	$0.15\lambda_g$	$11.10\lambda_g$	$0.71\lambda_g$	$0.06\lambda_g$
Resonant Frequency (MHz)	433	402	2400	433
Bandwidth (%)	3.2	35.9	18.64	33.9
Isolation (dB)	12.17	25.6	15.99	> 26
ECC	–	–	0.0025	0.1
Device level study?	No	No	No	Yes

elements. However, none of the reported studies considered these parameters. In addition, to the authors' knowledge, this is the first ever MIMO antenna system which is simulated and measured inside a quasi-implantable device.

IV. CONCLUSION

In this paper, a low-profile implantable MIMO antenna system is designed and experimentally validated for high data rate multi-purpose implantable devices. The proposed antenna exhibits compact size ($5.65^2 \times \pi \times 0.13 \text{ mm}^3$) with a minimum inter-element gap ($0.0018\lambda_g$) between MIMO elements. Moreover, the suggested antenna is integrated with electronic components of quasi-real implantable devices. The measurement is performed using minced pork meat, and saline solution and the results are found in good accordance with the simulated ones. Furthermore, the proposed antenna system has relatively good FBW (33.9%) and more compact size than recently reported implantable MIMO antennas. It has a maximum realized gain of -30 dBi and a high isolation of 26 dB. The main MIMO channel parameters are calculated and show good results. The ECC is less than 0.1, and DG is more than 9.95 dB in the operation band. Moreover, the transmission ability of the designed system is practically demonstrated through SDRs. The proposed work suggest that MIMO antenna system can be used to enhance channel capacity without any extra power and frequency resource for high data rate applications. The capability of supporting high data-rates make this antenna a promising option for high data-rate applications such as capsule endoscopy, live surgeries and any other biomedical applications.

REFERENCES

- [1] B. Biswas, A. Karmakar, and V. Chandra, "Miniaturised wideband ingestible antenna for wireless capsule endoscopy," *IET Microwaves, Antennas & Propagation*, vol. 14, no. 4, pp. 293–301, 2019.
- [2] M. Zada and H. Yoo, "Miniaturized dual band antennas for intra-oral tongue drive system in the ism bands 433 mhz and 915 mhz: Design, safety, and link budget considerations," *IEEE Transactions on Antennas and Propagation*, vol. 67, no. 9, pp. 5843–5852, 2019.
- [3] Z. Bao, Y.-X. Guo, and R. Mittra, "Single-layer dual-/tri-band inverted-f antennas for conformal capsule type of applications," *IEEE Transactions on Antennas and Propagation*, vol. 65, no. 12, pp. 7257–7265, 2017.
- [4] A. Basir and H. Yoo, "A stable impedance-matched ultrawideband antenna system mitigating detuning effects for multiple biotelemetric applications," *IEEE Transactions on Antennas and Propagation*, vol. 67, no. 5, pp. 3416–3421, 2019.

- [5] A. Basir and H. Yoo, "Efficient wireless power transfer system with a miniaturized quad-band implantable antenna for deep-body multitasking implants," *IEEE Transactions on Microwave Theory and Techniques*, vol. 68, no. 5, pp. 1943–1953, 2020.
- [6] A. Basir, M. Zada, Y. Cho, and H. Yoo, "A dual-circular-polarized endoscopic antenna with wideband characteristics and wireless biotelemetric link characterization," *IEEE Transactions on Antennas and Propagation*, vol. 68, no. 10, pp. 6953–6963, 2020.
- [7] A. Basir, A. Bouazizi, M. Zada, A. Iqbal, S. Ullah, and U. Naeem, "A dual-band implantable antenna with wide-band characteristics at mics and ism bands," *Microwave and Optical Technology Letters*, vol. 60, no. 12, pp. 2944–2949, 2018.
- [8] D. Miklavcic, N. Pavselj, and F. Hart, "Electric properties of tissues," *Wiley Encyclopedia of Biomed. Eng.*, ed. New York, NY, USA Wiley, Apr. 2006.
- [9] P. L. Poshtgol, L. Jichao, S. Soltani, and R. D. Murch, "Mimo antennas for capsule endoscope systems," in *2016 IEEE International Symposium on Antennas and Propagation (APSURSI)*. IEEE, 2016, pp. 1175–1176.
- [10] R. Tian, V. Plicanic, B. K. Lau, and Z. Ying, "A compact six-port dielectric resonator antenna array: Mimo channel measurements and performance analysis," *IEEE Transactions on Antennas and Propagation*, vol. 58, no. 4, pp. 1369–1379, 2010.
- [11] M. A. Jensen and J. W. Wallace, "A review of antennas and propagation for mimo wireless communications," *IEEE Transactions on Antennas and Propagation*, vol. 52, no. 11, pp. 2810–2824, 2004.
- [12] S. Xiao, C. Liu, Y. Li, X. M. Yang, and X. Liu, "Small-size dual-antenna implantable system for biotelemetry devices," *IEEE Antennas and Wireless Propagation Letters*, vol. 15, pp. 1723–1726, 2016.
- [13] Y. Fan, J. Huang, T. Chang, and X. Liu, "A miniaturized four-element mimo antenna with ebg for implantable medical devices," *IEEE Journal of Electromagnetics, RF and Microwaves in Medicine and Biology*, vol. 2, no. 4, pp. 226–233, 2018.
- [14] V. Kaim, B. K. Kanaujia, and K. Rambabu, "Quadrilateral spatial diversity circularly polarized mimo cubic implantable antenna system for biotelemetry," *IEEE Transactions on Antennas and Propagation*, pp. 1–1, 2020.
- [15] C. A. Balanis, *Antenna Theory: Analysis and Design*. John Wiley & Sons, 2016.
- [16] P.-L. Chi, R. Waterhouse, and T. Itoh, "Antenna miniaturization using slow wave enhancement factor from loaded transmission line models," *IEEE Transactions on Antennas and Propagation*, vol. 59, no. 1, pp. 48–57, 2010.
- [17] L. Riaz, U. Naeem, and M. F. Shafique, "Miniaturization of siw cavity filters through stub loading," *IEEE Microwave and Wireless Components Letters*, vol. 26, no. 12, pp. 981–983, 2016.
- [18] R. Das and H. Yoo, "A wideband circularly polarized conformal endoscopic antenna system for high-speed data transfer," *IEEE Transactions on Antennas and Propagation*, vol. 65, no. 6, pp. 2816–2826, 2017.
- [19] M. Alibakhshikenari, B. S. Virdee, C. H. See, R. Abd-Alhameed, A. H. Ali, F. Falcone, and E. Limiti, "Study on isolation improvement between closely-packed patch antenna arrays based on fractal metamaterial electromagnetic bandgap structures," *IET Microwaves, Antennas & Propagation*, vol. 12, no. 14, pp. 2241–2247, 2018.
- [20] D. Nikolayev, M. Zhadobov, L. L. Coq, P. Karban, and R. Sauleau, "Robust ultraminiature capsule antenna for ingestible and implantable applications," *IEEE Trans. Antennas Propag.*, vol. 65, no. 11, pp. 6107–6119, 2017.
- [21] A. Iqbal, A. Basir, A. Smida, N. K. Mallat, I. Elfergani, J. Rodriguez, and S. Kim, "Electromagnetic bandgap backed millimeter-wave mimo antenna for wearable applications," *IEEE Access*, vol. 7, pp. 111 135–111 144, 2019.
- [22] A. Basir, M. Zada, and H. Yoo, "Compact and flexible wideband antenna for intraoral tongue-drive system for people with disabilities," *IEEE Transactions on Antennas and Propagation*, vol. 68, no. 3, pp. 2405–2409, 2019.
- [23] M. Zada, I. A. Shah, A. Basir and H. Yoo, "Ultra-Compact Implantable Antenna with Enhanced Performance for Leadless Cardiac Pacemaker System," *IEEE Transactions on Antennas and Propagation*, doi: 10.1109/TAP.2020.3008070.
- [24] A. Iqbal, A. Smida, A. J. Alazemi, M. I. Waly, N. K. Mallat, and S. Kim, "Wideband circularly polarized mimo antenna for high data wearable biotelemetric devices," *IEEE Access*, vol. 8, pp. 17 935–17 944, 2020.
- [25] D. Gesbert, M. Shafi, D.-s. Shiu, P. J. Smith, and A. Nagueib, "From theory to practice: An overview of mimo space-time coded wireless systems," *IEEE Journal on Selected Areas in Communications*, vol. 21, no. 3, pp. 281–302, 2003.
- [26] P.-S. Kildal and K. Rosengren, "Correlation and capacity of mimo systems and mutual coupling, radiation efficiency, and diversity gain of their antennas: simulations and measurements in a reverberation chamber," *IEEE Communications Magazine*, vol. 42, no. 12, pp. 104–112, 2004.
- [27] Z. Li, Z. Du, M. Takahashi, K. Saito, and K. Ito, "Reducing mutual coupling of mimo antennas with parasitic elements for mobile terminals," *IEEE Transactions on Antennas and Propagation*, vol. 60, no. 2, pp. 473–481, 2011.



Amjad Iqbal (S'18) received the degree in Electrical Engineering from COMSATS University, Islamabad, Pakistan in 2016 and M.S degree in Electrical Engineering from the Department of Electrical Engineering, CECOS University of IT and Emerging Science, Peshawar, Pakistan in 2018. He worked as Lab Engineer at the Department of Electrical Engineering, CECOS University Peshawar from 2016 to 2018. He is pursuing PhD degree with the Faculty of Engineering, Multimedia University, Cyberjaya, Selangor, Malaysia. His research interests include

printed antennas, flexible antennas, implantable antennas, MIMO antennas, dielectric resonator antennas, wireless power transfer and synthesis of microwave components.



Muath Al-Hasan (M'10-SM'19) received his B.A.Sc. degree in electrical engineering from the Jordan University of Science and Technology, Jordan, in 2005, the M.A.Sc in wireless communications from Yarmouk University, Jordan in 2008, and the Ph.D. degree in Telecommunication engineering from Institut National de la Recherche Scientifique (INRS), Université du Québec, Canada, 2015. From 2013 to 2014, he was with Planetis Inc., California, USA. In May 2015, he joined Concordia University, Canada as postdoctoral fellowship. He is currently

an Assistant Professor with Al Ain University, United Arab Emirates. His current research interests include antenna design at millimeter-wave and Terahertz, channel measurements in Multiple-Input and Multiple-Output (MIMO) systems, and Machine Learning and Artificial Intelligence in antenna design.



Ismail Ben Mabrouk (M'07–SM'19) received the B.A.Sc. and M.A.Sc. degrees in Electrical Engineering from the University of Lille, Lille, France in 2006 and 2007, respectively and the Ph.D. in Electrical Engineering from University of Quebec, Canada, in 2012. From 2007 to 2009 he was with Huawei Technologies, Paris, France. In 2012, he joined the Wireless Devices and Systems (WiDeS) group at University of Southern California, Los Angeles, USA. He is currently an Assistant Professor at Durham University, Durham, UK. He is a recipient

of the Abu Dhabi Award for Research Excellence (AARE) – 2018. His research activities have been centred on antenna design at the millimeter-wave and THz frequencies, propagation studies for Multiple-Input and Multiple-Output (MIMO) systems, Deep Learning, and Wireless Body Area Network for medical applications.



Mourad Nedil (M'08-SM'12) received the Dipl. Ing. degree from the University of Algiers (USTHB), Algiers, Algeria, in 1996, the D.E.A (M.S.) degree from the University of Marne la Vallée, Marne la Vallée, France, in 2000, and the Ph.D. degree from the Institut National de la Recherche Scientifique (INRS-EMT), Université de Québec, Montréal, QC, Canada, in April 2006. He completed a Post-Doctoral Fellowship at INRS-EMT, within the RF Communications Systems Group, from 2006 to 2008. In June 2008, he joined the engineering School

department, University of Quebec at abitibi-Témiscamingue, Quebec, Canada, where he is now a full professor. His research interests include antennas, MIMO radio-wave propagation and microwave devices.